J. Plasma Phys. (2025), *vol*. 91, E132
 doi:10.1017/S0022377825100755

Dynamics of a collisional magnetized plasma sheath with non-thermal electrons, multi-component positive ions and charged dust: a fluid model analysis

Akshaya Kumar Shaw[1,2], Satyananda Kar[2] and P.V. Subhash[3,4]

[1]Institute for Plasma Research, Bhat, Gandhinagar 382 428, Gujarat, India
[2]Department of Energy Science and Engineering, Indian Institute of Technology Delhi, Hauz Khas, Delhi 110016, India
[3]ITER-India- Institute for Plasma Research, Bhat, Gandhinagar 382 428, Gujarat, India
[4]Homi Bhabha National Institute, Anushaktinagar, Mumbai 400094, Maharashtra, India

Corresponding author: Akshaya Kumar Shaw, akshayak@ipr.res.in

(Received 6 March 2025; revision received 28 July 2025; accepted 29 July 2025)

The properties of a collisional magnetized plasma sheath containing non-thermal electrons, multi-component ions (He^+ and Ar^+), neutral atoms and negatively charged dust particles are analysed. Using a one-dimensional fluid model, the parametric changes in sheath dynamics are investigated in the presence of nanometre-sized charged dust particles and an oblique magnetic field. The influence of charged dust, ionization, ion–neutral collisions, ion loss and non-thermal electrons on sheath parameters such as ion densities, velocities, electron density and potential is explored through theoretical modelling and numerical analysis. The results indicate that the ion density (He^+ and Ar^+) increases throughout the sheath region with rising ionization frequency in the absence of charged dust. However, when charged dust is present, the density of He^+ ions decreases while the density of Ar^+ ions increases, exhibiting a sharp peak near the sheath edge. It is also noted that the increase in ion–neutral collision frequency enhances the density, particularly near the sheath edge. Additionally, the presence of non-thermal electrons initially leads to an increase in ion density near the sheath edge, followed by a decrease within the sheath region. A qualitative explanation of the above phenomena, which occur due to different physical parameters, is provided.

Key words: plasma waves, dusty plasmas, plasma sheath

1. Introduction

The plasma sheath is a boundary layer that forms at the interface between a plasma volume and a solid surface or electrode. It plays a vital role in the interactions between the plasma and its boundaries (Franklin *et al*. 1970; Riemann 1991; Franklin 2003; Lieberman & Lichtenberg 2005; Riemann *et al*. 2005; Shaw *et al*.

2012). Understanding the characteristics and behaviour of plasma sheaths is crucial for various applications, including fusion energy research, semiconductor manufacturing, space propulsion systems, etc. The complexity of plasma sheaths increases significantly when multiple ion species are present (Riemann 1992, 2003; Foroutan 2010). Such multi-ion plasmas are common in various environments; for instance, fusion devices like tokamaks often use deuterium and tritium as fuel, creating a multi-ion plasma. Multiple ion species can significantly influence the distribution of the electric field, ion fluxes and the overall potential structure within the sheath (Shaw *et al*. 2024). Moreover, the presence of multiple ion species enhances the complexity of the plasma sheath primarily due to differences in their mass-to-charge ratios. These differences lead to species-specific responses to the sheath's electric fields, magnetic fields and ion–neutral collision, which further enhance the complexity of the sheath dynamics.

Introducing dust particles into the plasma further alters the system's behaviour, significantly impacting the sheath's properties and dynamics. In industrial applications, dusty plasmas use dielectric nanoparticles such as SiO_2 and Al_2O_3 (Merlino 2021) in the presence of ionized precursor gases. Depending on the process control mechanism, the plasma may contain single or multiple ion species. Dust particles and ions enter the sheath region, a phenomenon observed not only in laboratory experiments but also in naturally occurring dusty plasmas, such as in the solar system, planetary rings (Merlino 2006) and the Earth's magnetosphere. In the semiconductor industry, charged dust particles are significant, as gas mixtures like SiH_4 with O_2 and Ar are used in microelectronic fabrication. Similarly, carbon nanotubes and nanolayers are grown using CH_4 and H_2, with neutral species like He or Ar controlling plasma chemistry. Other applications involve multiple gases and ions, such as silicon wafer etching and Si–Ga–As semiconductor fabrication in radio frequency (RF) plasma. In Very Large-Scale Integration (VLSI) manufacturing, chemically reactive plasmas modify surfaces through etching or spoliation. The presence of dust outside semiconductor materials poses challenges, but moderate magnetic fields can influence the electron and ion dynamics for controlled deposition. Since dust grains do not easily magnetize in plasma, magnetic fields mainly affect electrons and ions, aiding pattern printing of semiconductors and circuits. Industrial applications include the growth of silicon nanoparticles, TiN thin films, carbon nanoparticles, molybdenum disulphide particles and synthetic diamond films. Strong Tesla-level magnetic fields in fusion devices cause dust generation from plasma-facing walls, altering core and edge plasma conditions. Dust species, such as carbon, tungsten, beryllium and hydrogen isotope ions, influence plasma behaviour, leading to wall erosion and re-deposition. Dust grain sizes range from nanometres to micrometres, making dust trapping an important research focus.

Several forces influence a charged dust particle, including neutral drag, ion drag, thermophoresis, gravitational force and radiation pressure. The thermionic, neutral and ion drag forces correspond to the square of the radius of the charged dust species. In contrast, the electric field's force exerted on the charged dust is directly proportional to its radius. Conversely, the gravitational force acting on the charged dust particles scales with the cube of their radius. The interplay of these forces creates a complex dynamics for charged dust particles, leading to various intriguing phenomena within the sheath (Shaw *et al*. 2023). In a magnetized plasma, charged particles are subjected to the Lorentz force, which modifies their paths and impacts the overall properties of the sheath (Sheridan & Goree 1991; Valentin 2000; Franklin 2005). Introducing non-thermal electrons, which have a velocity distribution that

https://doi.org/10.1017/S0022377825100755 Published online by Cambridge University Press

deviated from the Maxwellian profile (Fouial *et al.* 2016), adds another layer of complexity to the sheath dynamics. These non-thermal electrons often exhibit higher-energy tails, potentially affecting ionization rates and the energy distribution within the sheath.

Most theoretical and experimental studies on plasma sheaths consider various relevant parameters, including multiple positive and negative ion species, oblique magnetic fields, nanometre and micrometre-sized dust particles, ion–neutral collisions and electron distributions that follow either Boltzmann or non-Boltzmann statistics (Resendes, Sorasio & Shukla 2002; Hatami *et al*. 2008; Dubinov 2009; Hatami, Shokri & Niknam 2009; Chekour, Tahraoui & Zaham 2012; Foroutan & Akhoundi 2012; Shaw *et al*. 2012; Hatami 2015; Ou *et al*. 2015). For instance, Raffah *et al*. (2024) examined the surface potential of dust particles in an argon–helium plasma using the (r, q)-distribution function, where r parameter describes the flatness of the electron distribution at low energies and q parameter describes the superthermal (high-energy) tail of the distribution. Their study analysed how parameters such as the distribution function indices, ion-to-electron temperature ratios and ion number density ratios affect the charging of dust particles. Fouial *et al*. (2016) investigated the Bohm criterion in dusty plasmas containing two positive ion species and non-thermal electrons. This study derived a generalized Bohm criterion for a low-pressure, one-dimensional, un-magnetized argon–helium plasma with dust particles, highlighting how multi-ion species influence sheath formation and the ion dynamics. Maiorov *et al*. (2015) studied the impact of gas composition on plasma-dust structures in RF discharges. Their research demonstrated significant changes in the correlation characteristics of dust particles due to small amounts of argon, supported by numerical simulations. These findings have significant implications for industrial applications, including plasma-aided material processing, nanostructure thin film deposition, plasma etching in microelectronics and fusion devices.

The individual physics of collisional electrostatic, magnetized and dusty plasma sheaths has been well explored in the literature, each highlighting specific mechanisms that influence sheath formation. The role of collisions, particularly ion–neutral interactions, in shaping the sheath profile and modifying the Bohm criterion has been systematically analysed by Riemann (1997), showing that increased collisionality broadens the sheath and alters ion energy distributions. The effects of magnetic fields on sheath structure, including sheath narrowing, field-aligned asymmetry and orientation-dependent behaviour, are investigated in works such as Singha, Sarma & Chutia (2001) and Zou *et al*. (2004), demonstrating that magnetic confinement significantly affects plasma–wall interaction and the particle dynamics. The physics of dusty sheaths, involving dust charging, force balance (electrostatic, gravitational, ion drag) and equilibrium positions, has been comprehensively addressed in studies like Liu, Wang & Ma (2000) and Zhao, Zhang & Wang (2020).

Most studies have focused on collisionless plasma environments. However, in actual laboratory and astrophysical settings, weakly ionized and collisional plasma models are often more applicable. Observations and experimental data have therefore motivated significant research into how ionization influences nonlinear structures within these collisional plasma models (Mehdipoor *et al*. 2010; Tamang *et al*. 2018).

Ionization plays a crucial role at the plasma boundary, as it generates the ions necessary for sheath formation (Dhawan & Malik 2023). The Bohm criterion, which governs ion flow velocity and determines the sheath entrance, has been modified for collisional, un-magnetized plasmas by incorporating an ionization source term

https://doi.org/10.1017/S0022377825100755 Published online by Cambridge University Press

(El Bojaddaini & Chayei 2020). Additionally, ionization can deplete thermal electrons, causing the electron distribution to deviate from a Maxwellian profile. Chen *et al*. (2023) examined sheath formation and structure with various ionization source terms in collisional, magnetized, non-extensive plasma. Furthermore, using different collisional models, studies have investigated sheath properties and dust charging processes in weakly ionized, magnetized dusty plasmas.

In collisional dusty plasma sheaths, electrons, due to their higher mobility compared with ions, often fail to reach thermal equilibrium under low-density conditions. To address complex physical problems involving highly energetic particles, researchers have focused on systems that deviate from thermal equilibrium. This has led to significant interest in studying plasma sheaths with non-Maxwellian distributions, such as the Cairns–Tsallis (Ou & Men 2020), non-extensive (El Bojaddaini & Chayei 2020, kappa (Sadatian & Ghiyaei 2021), Cairns (Khalilpour & Foroutan 2020) and cutoff Maxwellian (Basnet, Sarma & Khanal 2020) distributions. Notably, the distribution function introduced by Cairns *et al*. (1995) has been proven effective in modelling non-thermal electrons and explaining the nonlinear phenomena observed by the Viking spacecraft and Freja satellites (Bostrom 1992). This distribution also converges to the conventional Maxwell–Boltzmann distribution in limiting cases.

The combined presence of non-thermal electrons and dust grains in a multicomponent plasma has a unique and profound impact on the plasma sheath. However, the influence of these factors on the sheath behaviour of a collisional plasma with an ionization source, ion loss and multiple positive ion species remains underexplored. This study aims to address this gap by investigating sheath characteristics such as ion densities, electron density, ion velocities, sheath potential, space charge and ion current for both with and without charged dust and magnetic fields. The effects of electron impact ionization and ion loss within the sheath are also considered. Furthermore, we examine how these sheath characteristics vary with changes in external magnetic field strength, ion–neutral collision frequency and the population of non-thermal electrons. Section 2 presents the nonlinear basic model equations for different plasma species; the dimensionless equations are given in § 3, followed by a detailed analysis of the results in § 4 and a brief conclusion is provided in § 5.

2. Basic equations

In this research, we considered a low-pressure plasma mixture of two types of positive ions (He^+ and Ar^+), non-thermal electrons and nano-scale dust particles with a mass density of 2×10^3 kg m^{-3}, introduced externally into the system (Franklin 2003; Mehdipour *et al*. 2010). We have analysed the plasma in a one-dimensional (1-D) spatial coordinate within phase space, considering 3-D velocity components v_x, v_y and v_z, as illustrated in figure 1. However, the physical parameters of the sheath are permitted to vary only in the direction perpendicular to the surface, specifically along the z-axis.

To examine the behaviour of the plasma sheath dynamics and the distribution of ion densities and velocities in the sheath domain, we utilized a multi-fluid model. We assumed that neutral gas particles are evenly dispersed across the sheath zone and remain largely stationary compared with the drift of ions and electrons in both magnetized and un-magnetized plasmas. The collision cross-sections for He^+ and Ar^+ ions interacting with neutral particles were determined based on their respective temperatures. When electrons are accelerated to speeds approaching their thermal

https://doi.org/10.1017/S0022377825100755 Published online by Cambridge University Press

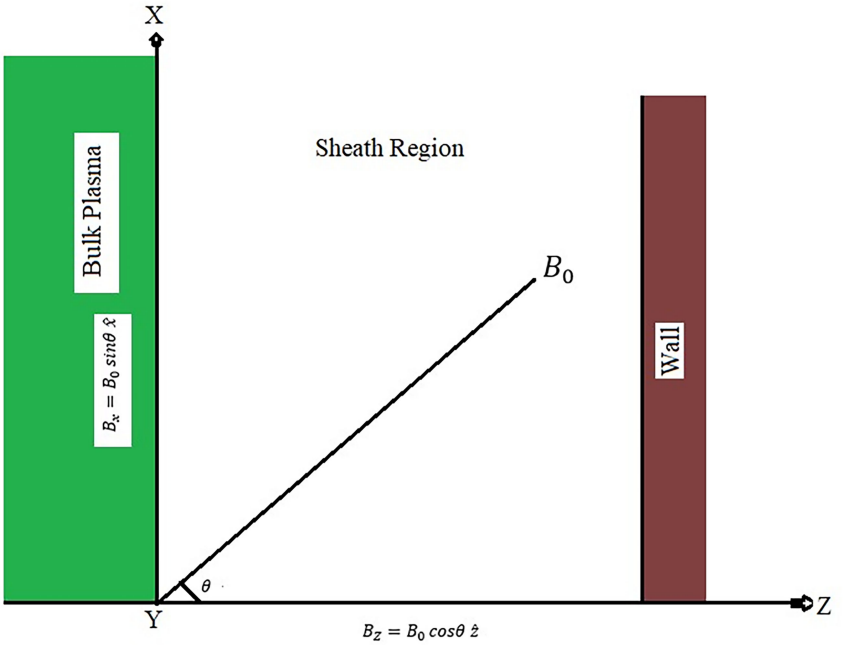

FIGURE 1. Geometrical model for magnetized plasma sheath.

velocities, electron inertia becomes significant. In these cases, the electron fluid cannot be accurately represented by the Boltzmann relation and instead follows the Cairns (Fouial *et al*. 2016) distribution, with the electron distribution function expressed as (Cairns *et al*. 1995)

$$f_e(v) = \frac{n_{e0}}{(3\alpha+1)\sqrt{2\pi v_{the}^2}}\left(1+\frac{\alpha v^4}{v_{the}^4}\right)\exp\left(-\frac{v^2}{2v_{the}^2}\right), \tag{2.1}$$

where v is the electron velocity, n is electron density, $v_{the} = \sqrt{T_e/m_e}$ is the electron thermal velocity and T_e and m_e are the electron temperature and mass respectively. The parameter α indicates how much the distribution deviates from a Maxwellian distribution. It is clear that as α approaches 0, the distribution converges to the Maxwellian form, as shown in figure 2. Analysis of figure 2 demonstrates that, as α increases, there is a corresponding rise in the population of high-energy tail electrons. This indicates that the parameter α directly influences the generation of energetic electrons in the suprathermal region of the distribution. From (2.1) we can determine the electron density by integrating it and replacing $(v^2)/(v_{the}^2)$ by $(v^2)/(v_{the}^2) - 2(\phi/T_e)$

$$n_e = \int f_e(v)\,\mathrm{d}v = n_{e0}\left[1 - b\left(\frac{e\phi}{T_e}\right) + b\left(\frac{e\phi}{T_e}\right)^2\right]\exp\left(\frac{e\phi}{T_e}\right),$$

$$b = \frac{4\alpha}{(1+3\alpha)}. \tag{2.2}$$

The parameter α represents the proportion of non-thermal electrons in the system. When $b = 0$ (i.e. $\alpha = 0$), (2) corresponds exclusively to the Maxwellian distribution, where ϕ and n_{e0} are the potential and electron density at the sheath edge respectively.

https://doi.org/10.1017/S0022377825100755 Published online by Cambridge University Press

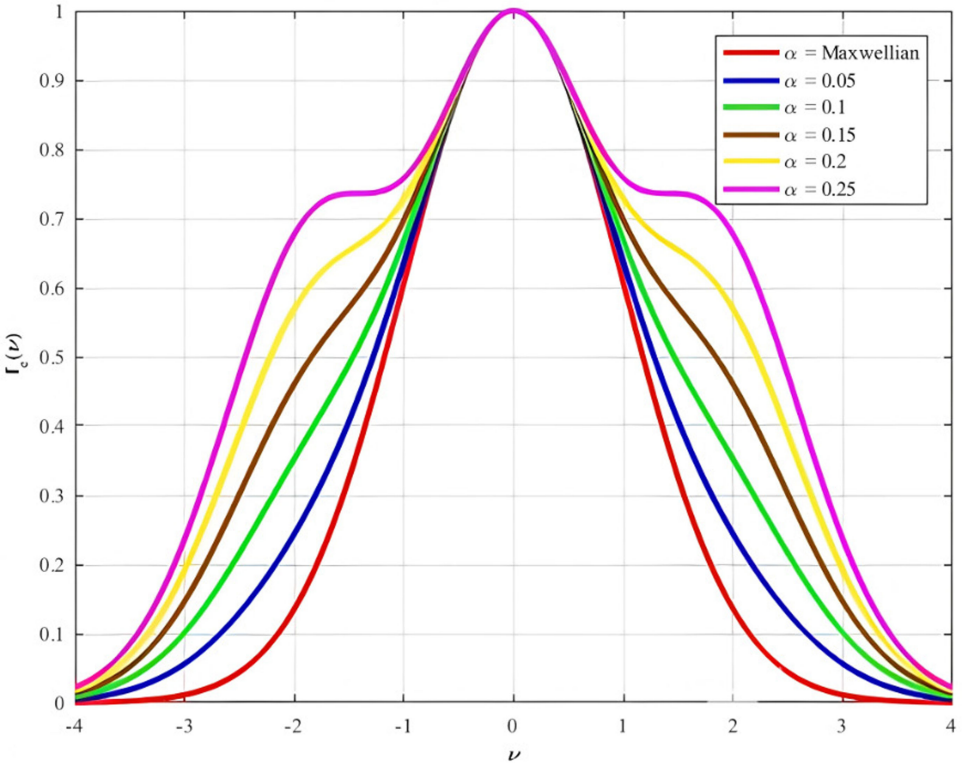

FIGURE 2. Non-thermal electron distribution function $f_e(\nu)$ given in (2.1).

The quasi-neutrality conditions are satisfied at the sheath edge and expressed as

$$n_{10} + n_{20} = q_{d0} n_{do} + n_{e0}, \tag{2.3}$$

where n_{10}, n_{20} and n_{do} are the He^+ ion, Ar^+ ion and charged dust density at the sheath edge, respectively, and q_{d0} is the dust charge number at the sheath edge.

In a steady-state scenario, where ionization, ion loss and collisions are present, the behaviour of positive thermal ions is described by the continuity and momentum equations

$$u_i \frac{\mathrm{d}n_i}{\mathrm{d}z} + n_i \frac{\mathrm{d}u_i}{\mathrm{d}z} = \nu_{iz} n_e - \nu_{il} n_i, \tag{2.4}$$

$$u_d \frac{\mathrm{d}n_d}{\mathrm{d}z} + n_d \frac{\mathrm{d}v_d}{\mathrm{d}z} = 0, \tag{2.5}$$

$$\begin{aligned} m_i n_i (u_i.\nabla) u_i = &-e n_i \nabla\phi + e n_i (u_i \cdot B) - \nabla p_i - m_i n_i u_i \nu_{in} - m_i u_i \nu_{iz} n_e \\ &- m_i n_i \left(u_{iz} - u_{\mathrm{d}z}\right) \nu_{id}, \end{aligned} \tag{2.6}$$

$$m_d n_d u_d \cdot \nabla u_d = -q_d n_d \nabla\phi + q_d n_d V_d \cdot B + \sum_{i=1,2} F_{id} + F_{nd}, \tag{2.7}$$

where $i = 1, 2$ correspond to the lighter ion (He^+) and heavier ion (Ar^+) respectively. Also, m_i, m_d, n_i, n_d, u_i and u_d are the mass of ions and dust, density of

https://doi.org/10.1017/S0022377825100755 Published online by Cambridge University Press

ions and dust and velocity of ions and dust species, respectively, B is the magnetic field that makes an angle θ with the z axis $B = B_0(\hat{z}\cos\theta + \hat{x}\sin\theta)$, as shown in figure 1, ν_{iz} and ν_{il} are the ionization frequency and ion loss frequency (Ivlev & Morfill 2000), respectively and ν_{in} and ν_{id} represent the ion–neutral and ion–dust collision frequencies, respectively. In the theoretical study of solitary waves in collisional dusty plasmas, the unperturbed particle densities adhere to the condition $\nu_{iz}n_{e0} - \nu_{il}n_{i0} = 0$ (Misra & Chowdhury 2004). However, to examine the impact of ionization, we assumed the ionization frequency was higher than the ion loss frequency. The parameter $p_i = K_B T_i n_i$, represents the partial pressure of positive ions, where, K_B is the Boltzmann constant, T_1 is the He^+ion temperature and T_2 is the Ar^+ ion temperature.

Using Poisson's equation, we relate the number densities of ions, electrons and dust to the electric potential under equilibrium conditions

$$\nabla^2\phi = -\frac{e}{\varepsilon_0}\left(n_1 + n_2 - q_d n_d - n_e\right). \tag{2.8}$$

Using magnetic field inclination, the above equation (2.6) and (2.7) can be written as

$$m_i u_{iz}\frac{\mathrm{d}u_{ix}}{\mathrm{d}z} = eB_0\cos\theta u_{iy} - m_i n_i u_i \nu_{in} - m_i u_i \nu_{iz} n_e, \tag{2.9}$$

$$m_i u_{iz}\frac{\mathrm{d}u_{iy}}{\mathrm{d}z} = eB_0\left[\sin\theta u_{iz} - \cos\theta u_{ix}\right] - m_i n_i u_i \nu_{in} - m_i u_i \nu_{iz} n_e, \tag{2.10}$$

$$m_i u_{iz}\frac{\mathrm{d}u_{iz}}{\mathrm{d}z} = -e\frac{\mathrm{d}\phi}{\mathrm{d}z} - eB_0\sin\theta u_{iy} - \frac{T_j}{n_1}\frac{\mathrm{d}n_1}{\mathrm{d}z} - m_i n_i u_i \nu_{in} - m_i u_i \nu_{iz} n_e - m_i\left(u_{iz} - u_{dz}\right)\nu_{id}, \tag{2.11}$$

$$m_d u_{\mathrm{d}z}\frac{\mathrm{d}u_{\mathrm{d}x}}{\mathrm{d}z} = q_d B_0\cos\theta u_{\mathrm{d}y} + F_{id} + F_{nd}, \tag{2.12}$$

$$m_d u_{\mathrm{d}z}\frac{\mathrm{d}u_{\mathrm{d}y}}{\mathrm{d}z} = q_d B_0\left[\sin\theta u_{\mathrm{d}z} - \cos\theta u_{\mathrm{d}x}\right] + + F_{id} + F_{nd} + F_G + F_{EM}, \tag{2.13}$$

$$m_d u_{\mathrm{d}z}\frac{\mathrm{d}u_{\mathrm{d}z}}{\mathrm{d}z} = -q_d\frac{\mathrm{d}\phi}{\mathrm{d}z} - q_d B_0\sin\theta u_{dy} + F_{id} + F_{nd} + F_G + F_{EM}, \tag{2.14}$$

where F_{EM}, F_G, F_{nd} and F_{id} are the electromagnetic, gravitational, neutral drag and ion drag forces, respectively. To determine the dust charge q_d (which corresponds to the dust surface potential, $\varnothing_d$) in the equations mentioned above, we presumed that the dust charging time is shorter than the characteristic time of dust motion since the charging process is a localized aspect (Franklin 2003). When a neutral dust particle enters the plasma, it progressively gains charge by collecting electrons and ions, following the governing equation

$$\frac{\mathrm{d}q_d}{\mathrm{d}t} = \sum_{i=1,2} I_i + I_e. \tag{2.15}$$

The electron and ion currents to the dust particles, denoted as I_i and I_e, can be determined using orbit motion limited theory (Tang & Delzanno 2014). In this

https://doi.org/10.1017/S0022377825100755 Published online by Cambridge University Press

study, we assume that the distance between dust particles is greater than the ion Debye length, which allows us to apply dust charging theory. Additionally, we consider a maximum magnetic field strength of approximately 1.5 T and a dust radius of 4×10^{-8} m. Under such magnetic conditions, the electron gyro-radius ($\rho_e = v_{te}/\Omega_e$, $\Omega_e = eB_{0/m_e}$) is calculated to be 2.249×10^{-6} m. Since the electron gyro-radius is significantly larger than the dust radius ($\rho_e \gg r_d$) (Foroutan 2010), the magnetic field has a negligible effect on the dust charging process and is therefore ignored in our analysis. To achieve charge equilibrium, we set $(\mathrm{d}q_d)/(\mathrm{d}t) = 0$ in (2.14), resulting in the steady-state potential and charge

$$I_e = -\pi r_d^2 e \left(\frac{8T_e}{\pi m_e}\right)^{1/2} n_e \exp\left(\frac{eq_d}{r_d T_e}\right), \tag{2.16}$$

$$\sum_{i=1,2} I_i = \pi r_d^2 e n_j v_j \left(1 - \frac{2eq_d}{r_d m_j v_j^2}\right), \tag{2.17}$$

for $(\mathrm{d}q_\mathrm{d})/(\mathrm{d}t)$ and

$$I_e = -\pi r_d^2 e \left(\frac{8T_e}{\pi m_e}\right)^{1/2} n_e \left(1 + \frac{eq_d}{r_d T_e}\right), \tag{2.18}$$

$$\sum_{i=1,2} I_i = \pi r_d^2 e n_j v_j exp \left(\frac{2eq_d}{r_d m_j v_j^2}\right), \tag{2.19}$$

for $q_d > 0$.

Near the sheath edge, positive ions accelerate toward the wall, reaching a directed velocity that may be comparable to their thermal velocity. To apply the orbital motion limited theory in this region, the ion velocity must be replaced with the effective mean velocity of ions moving toward the dust particles. For a spherical dust particle, the charge q_d can be expressed in terms of the dust surface potential as $q_d = r_d \phi_d$, where ϕ_d represents the dust surface potential. The dust charge q_d is determined by using the dust particle's current balance equation, $I_e = \sum_{i=1,2} I_i$.

Once the dust becomes charged, it experiences different forces due to electricity being charged and its own mass. The net force on the charged dust particle can be expressed as

$$m_d \frac{\mathrm{d}v_d}{\mathrm{d}t} = F_{EM} + F_G + F_D + F_T + F_p. \tag{2.20}$$

The electromagnetic force arises from the combined effects of electric and magnetic forces. The ion drag force on dust particles primarily results from momentum transfer during ion–dust interactions, whereas the neutral drag force stems from interactions between neutral particles and dust. The ion drag force influencing dust particles can be divided into two components: (i) direct ion collection by dust particles and (ii) ion scattering within their electrostatic field. The expressions for these forces are given below

$$\sum_{j=1,2} F_{\text{collecton}} = \pi r_d^2 n_j m_j v_{sj} \widetilde{v_j} \left(1 - \frac{2eq_d}{r_d m_j v_{sj}^2}\right), \tag{2.21}$$

$$\sum_{j=1,2} F_{\text{coulomb}} = 2\pi b_0^2 n_j m_j v_{sj} \widetilde{v_j} ln \left(\frac{b_0^2 + \lambda_D^2}{b_0^2 + b_c^2}\right). \tag{2.22}$$

https://doi.org/10.1017/S0022377825100755 Published online by Cambridge University Press

Here, $v_{sj} = \sqrt{(\check{v}_j^2 + 8T_j/\pi m_j)}$ represents the mean ion velocity, and $\tilde{v}_j = (v_j - v_d)$ is the ion velocity relative to the dust particles. The impact radius for a 90^0 deflection is given by $b_0 = (r_d T_e/(m_j v_j^2))$, while the direct collision impact parameter is $b_c = r_d\sqrt{(1 - 2b_0/r_d)}$. The Debye length of the plasma is expressed as $\lambda_D = \lambda_{De}\lambda_{Dj}/\sqrt{(\lambda_{De}^2 + \lambda_{Dj}^2)}$ and the Debye lengths for electrons and ions are ($\lambda_{De} = (\varepsilon_0 T_e/n_{e0}e^2)^{1/2}$) and $\lambda_{Dl} = (\varepsilon_0 T_j/n_{j0}e^2)^{1/2}$ ($j = 1, 2$), respectively.

For a typical dust radius, $r_d \ll \lambda_{mfp}$ and the velocity $v_d \ll v_{th,n}$, where $v_{th,n} = \sqrt{T_n/m_n}$ (with T_n and m_n being the temperature and mass of neutral gas, respectively), and $\lambda_{mfp} = 1/\sqrt{2\pi r_d^2 n}$. The neutral drag force can be expressed as follows:

$$F_{nd} = -\chi\frac{4}{3}\pi r_d^2 m_n n_n v_{thn} v_d. \tag{2.23}$$

Here, $\chi = 1$ corresponds to specular reflection, while $\chi = 1.442$ applies to diffuse reflection. The parameter v_{thn} represents the thermal velocity of the neutral gas, and n_n denotes the neutral gas density. The gravitational force acting on the dust species is given by

$$F_G = m_d g = \frac{4}{3}\pi r_d^3 \rho_d g, \tag{2.24}$$

where ρ_d represents the mass density of the dust species and g represents the acceleration due to gravity.

Additionally, the electromagnetic forces F_{EM} acting on moving charged dust particles with charge q_d is the combined effect of the electric field and the Lorentz force, expressed as follows:

$$F_{EM} = F_E + F_M, \tag{2.25}$$

$$F_E = q_d \cdot E, \tag{2.26}$$

$$F_M = q_d v_d \cdot B. \tag{2.27}$$

Here, E denotes the electric field, B represents the magnetic field.

To validate the dusty plasma sheath, the dust radius (r_d), impact radius (b_0) and electron Debye length (λ_{De}) must follow $\lambda_{De} > b_0 > r_d$. The conventional values estimated are $\lambda_{De} = 3.36 \times 10^{-4}$ m, $b_0 = 1.2 \times 10^{-7}$ m for $r_d = 4 \times 10^{-8}$ m. This confirms that the sheath assessment in dusty plasma is satisfied. For a standard dust oscillation frequency of 15 Hz (Kong *et al*. 2016) and taking into account the dust acoustic speed of 20 cm s^{-1}, we calculated the dust acoustic wavelength to be 0.19 cm, indicating that the phase velocity is comparable to the dust acoustic speed. Additionally, we estimated the dust thermal speed to be 2.4 cm s^{-1}. Therefore, we conclude that the fluid approximation is valid within our specified range of parameters.

3. Dimensionless equations

For a better understanding of the momentum and continuity equations for the ions and dust, the following dimensionless variables are introduced: $N_1 = n_1/n_{10}$, $N_2 = n_2/n_{20}$, $N_d = n_d/n_{d0}$ and $N_e = n_e/n_{e0}$, $\psi = -e\phi/t_e$, $T_{i1} = T_1/T_e$, $T_{i2} = T_2/T_e$, $\mu = \mathrm{m_1/m_2}$, $\mu_1 = \mathrm{m_1/m_d}$, $\mathrm{U}_{i,x,y,z} = \mathrm{u}_{i,x,y,z}/\mathrm{c_{si}}$, $U_{d,x,y,z} = u_{d,x,y,z}/c_{sd}$, $\nu_{Li} = (\nu_{Li}\lambda_{Di})/(C_{si}\nu_{id})$, $\sigma_i = (\nu_{iz}\lambda_{Di})/(C_{si})$, $\varepsilon_i = (\nu_{in}\lambda_{Di})/(C_{si})$, $\lambda_{Di} = ((T_e)/(n_{io}e^2))^{1/2}$,

https://doi.org/10.1017/S0022377825100755 Published online by Cambridge University Press

$Z_d = q_d/e$, $\upsilon_{id} = (\upsilon_{id}\lambda_{Di})/(C_{sd})$, $\gamma = \lambda_{De}/m_d c_{sd}^2$, $\beta = \omega_{ci}/\omega_{pi}$, $\omega_{ci} = eB_0/m_i$ and, $\omega_{pi} = (n_i e^2/\varepsilon_0 m_i)^{1/2}$, $c_{sd} = (Z_d T_e/m_d)^{1/2}$, $\zeta = z/\lambda_{De}$. Using above dimensionless parameters in (3.1)–(3.14), we may write

$$N_e = \left[1 - b\,(\psi) + b\,(\psi)^2\right] \exp\,(\psi)\,, \tag{3.1}$$

$$N_1 \frac{\mathrm{d}U_{1z}}{\mathrm{d}\zeta} + U_{1z}\frac{\mathrm{d}N_1}{\mathrm{d}\xi} = \sigma_1 N_e - \nu_{L1} N_1, \tag{3.2}$$

$$N_2 \frac{\mathrm{d}U_{2z}}{\mathrm{d}\zeta} + U_{2z}\frac{\mathrm{d}N_2}{\mathrm{d}\zeta} = \sigma_2 N_e - \nu_{L2} N_2, \tag{3.3}$$

$$N_d \frac{\mathrm{d}U_{\mathrm{dz}}}{\mathrm{d}\zeta} + U_{\mathrm{dz}}\frac{\mathrm{d}N_{\mathrm{d}}}{\mathrm{d}\zeta} = 0, \tag{3.4}$$

$$U_{1z}\frac{\mathrm{d}U_{1x}}{\mathrm{d}\zeta} = \beta U_{1y}\cos\theta - \frac{\sigma_1 U_{1x}}{N_1}\left(N_e + \frac{\varepsilon_1}{\sigma_1}N_1\right), \tag{3.5}$$

$$U_{1z}\frac{\mathrm{d}U_{1y}}{\mathrm{d}\zeta} = \beta\left[\sin\theta U_{1z} - \cos\theta U_{1x}\right] - \frac{\sigma_1 U_{1y}}{N_1}\left(N_e + \frac{\varepsilon_1}{\sigma_1}N_1\right), \tag{3.6}$$

$$U_{1z}\frac{\mathrm{d}U_{1z}}{\mathrm{d}\zeta} = \frac{\mathrm{d}\psi}{\mathrm{d}\zeta} - \frac{T_{i1}}{N_1}\frac{\mathrm{d}N_1}{\mathrm{d}\xi} - \beta\sin\theta U_{1y} - \frac{\sigma_1 U_{1z}}{N_1}\left(N_e + \frac{\varepsilon_1}{\sigma_1}N_1\right) - (U_{1z} - U_{\mathrm{dz}})\,\upsilon_{1d}, \tag{3.7}$$

$$U_{2z}\frac{\mathrm{d}U_{2x}}{\mathrm{d}\zeta} = \mu\beta U_{2y}\cos\theta - \frac{\sigma_2 U_{2x}}{N_2}\left(N_e + \frac{\varepsilon_2}{\sigma_2}N_2\right), \tag{3.8}$$

$$U_{2z}\frac{\mathrm{d}U_{2y}}{\mathrm{d}\zeta} = \mu\beta\left[\sin\theta U_{2z} - \cos\theta U_{2x}\right] - \frac{\sigma_2 U_{2y}}{N_2}\left(N_e + \frac{\varepsilon_2}{\sigma_2}N_2\right), \tag{3.9}$$

$$U_{2z}\frac{\mathrm{d}U_{2z}}{\mathrm{d}\zeta} = \mu\frac{\mathrm{d}\psi}{\mathrm{d}\xi} - \mu\frac{T_{i2}}{N_2}\frac{\mathrm{d}N_2}{\mathrm{d}\zeta} - \mu\beta\sin\theta U_{2y} - \frac{\sigma_2 U_{2z}}{N_2}\left(N_e + \frac{\varepsilon_2}{\sigma_2}N_1\right) - (U_{2z} - U_{\mathrm{dz}})\,\upsilon_{2d}, \tag{3.10}$$

$$U_{\mathrm{dz}}\frac{\mathrm{d}U_{\mathrm{dx}}}{\mathrm{d}\zeta} = Z_d\mu_1\beta\cos\theta U_{dy} + \gamma\left(\sum_{i=1,2} F_{id} + F_{nd}\right), \tag{3.11}$$

$$U_{\mathrm{dz}}\frac{\mathrm{d}U_{\mathrm{dy}}}{\mathrm{d}\zeta} = Z_d\mu_1\beta\left[\sin\theta U_{\mathrm{dz}} - \cos\theta U_{\mathrm{dx}}\right] + \gamma\left(\sum_{i=1,2} F_{id} + F_{nd}\right), \tag{3.12}$$

$$U_{\mathrm{dz}}\frac{\mathrm{d}U_{\mathrm{dz}}}{\mathrm{d}\zeta} = Z_d\mu_1\frac{\mathrm{d}\psi}{\mathrm{d}\xi} - \beta\mu_1\sin\theta U_{\mathrm{dy}} + \gamma\left(\sum_{i=1,2} F_{id} + F_{nd}\right), \tag{3.13}$$

$$\frac{\mathrm{d}^2\psi}{\mathrm{d}\zeta^2} = \left[N_1 + N_2 - Z_d N_d - N_e\right]. \tag{3.14}$$

https://doi.org/10.1017/S0022377825100755 Published online by Cambridge University Press

4. Numerical results and discussion

In this section, we presented the findings from a numerical simulation of the coupled nonlinear differential equations that describe a magnetized plasma sheath containing two types of positive ions, non-thermal electrons and negatively charged dust particles. We have estimated the forces acting on the dust species as follows: collection force, 7.89×10^{-9} N; collisional force, 4.83×10^{-10} N; neutral drag force, 7.03×10^{-16} N; electromagnetic force, 5.38×10^{-18} N; and gravitational force, 5.2518×10^{-18} N. Both gravitational and electromagnetic forces are balanced to enable dust levitation. In our analysis, these forces are relatively small and thus neglected. Instead, we focus on the drag force, which is the most significant for charged dust species.

At the start of this section, we note that weakly ionized plasmas imply the presence of finite numbers of neutral particles in the model, necessitating the consideration of ion–neutral collisions, ion loss and ionization effects. Using the fourth-order Runge–Kutta method in MATLAB and an appropriate initial value, (3.1)–(3.14) are solved with the step size 0.0003. For our calculations, we used the initial values. The densities of electrons, He^+ ions, Ar^+ ions and dust are $n_e = 1 \times 10^{15}$, $n_1 = 0.6 \cdot n_e$, $n_2 = 0.4 \cdot n_e$ and $n_d = 1 \times 10^{11}\ \mathrm{m}^{-3}$, respectively. The temperature of electrons, ions and dust are, $T_e = 3$, $T_1 = 0.13$, $T_2 = 0.05$ and $T_d = 0.003$ eV (Mand & Mashayek 2005), respectively. The ion–neutral collision cross-sections of Ar^+ and He^+ ions (Foroutan 2010) are 5×10^{-15} and $1.6 \times 10^{-15}\ \mathrm{cm}^2$ respectively. The initial normalized velocities of He^+ ions, Ar^+ ions and dust particles along the z-axis are $U_{1,z}(\xi = 0) = 1.0$, $U_{2,z}(\xi = 0) = 0.2$ and $U_{d,z}(\xi = 0) = 0.054$, other velocity components of He^+ ions, Ar^+ ions and dust particles along the x and y axes are taken as zero. At the sheath edge ($\xi = 0$), the potential is zero ($\psi = 0$), however, to avoid numerical divergence we assume that $(\mathrm{d}\psi(\xi = 0))/(\mathrm{d}\xi)$ takes an infinitesimal value of 0.001.

4.1. *Ion density and velocity with and without charged dust and ionization effect*

Our model considered a composition consisting of a ratio of 60 % He^+ and 40 % Ar^+ ions concerning the electron plasma density inside the sheath vicinity. Figures 3, 4, 5, 6 and 7 illustrate the effects of electron impact ionization in the presence and absence of charged dust particles. Figures 3 and 4 precisely depict the normalized ion densities of He^+ and Ar^+ ions, respectively, as a function of the normalized distance from the sheath edge. It is evident from both figures that, as the normalized ionization frequency (σ) increases, the ion density of both species also increases. However, the amplitude of the density peaks differs between the ions due to the higher ionization rate of Ar^+ compared with He^+ ions, which can be determined from their respective ionization rate equations: $R_{\mathrm{He}} = k_{\mathrm{He0}} n_e n_n \exp((-24.6)/(k_b t_e))$ for He^+ and $R_{\mathrm{Ar}} = k_{\mathrm{Ar0}} n_e n_n \exp((-15.76)/(k_b t_e))$ for Ar^+ ions, respectively.

When charged dust enters the sheath, the He^+ ion density decreases, whereas the Ar^+ ion density increases. This occurs because the magnitude of the dust charge near the sheath edge is significantly higher when He^+ ions are dominant. This is due to the fact that He^+ ions, with their smaller size, yield a larger dust charging current compared with Ar^+ ions, resulting in a greater absolute dust charge in the vicinity of the sheath edge. Additionally, the ion loss frequency of He^+ ions is higher than that of Ar^+ ions. The ion current ratio profile (figure 5), which compares the He^+ ion current with the Ar^+ ion current, demonstrates that the He^+ ion current decreases rapidly from the sheath edge to the wall, whereas the

https://doi.org/10.1017/S0022377825100755 Published online by Cambridge University Press

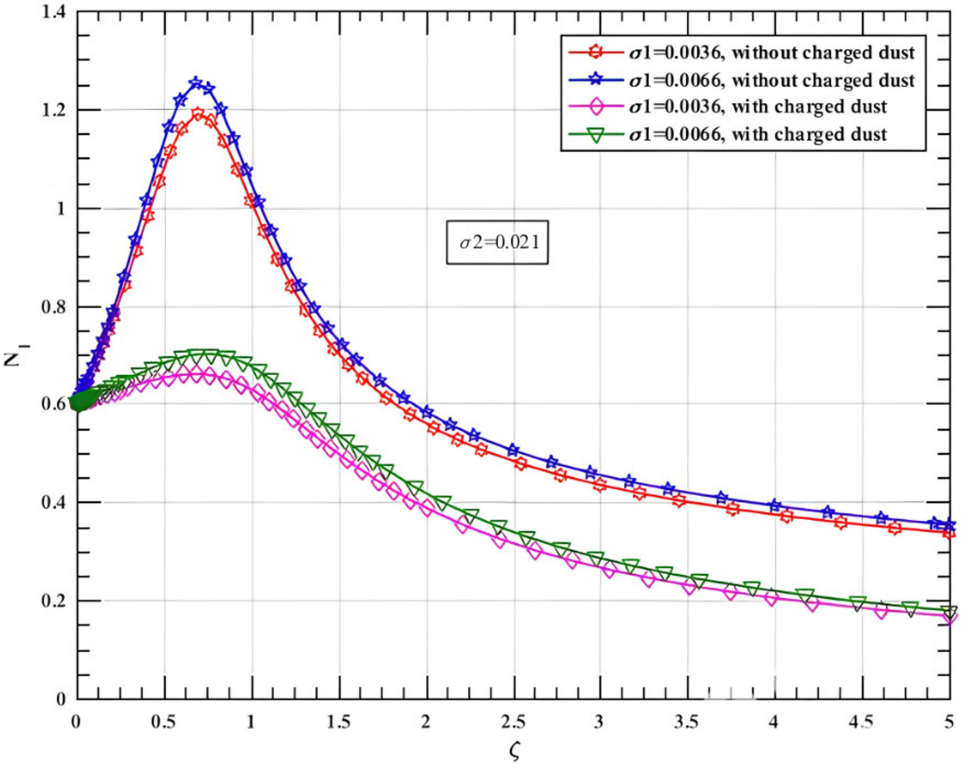

FIGURE 3. Variation of normalized He^+ ion density with normalized distance for different values of σ, for $\beta = 0.5$, $\theta = 10°$, $T_e = 3$eV, $T_1 = 0.13$eV, $T_2 = 0.05$eV, $T_d = 0.003$eV.

Ar^+ ion current declines more gradually. Therefore, in the presence of charged dust, the density of He^+ ions decreases while the density of Ar^+ ions increases.

The accumulation of ions near the sheath edge arises from a partial breach of the quasi-neutrality condition within the sheath. An electric field, that is dependent on the sheath's thickness, forms and grows more substantial from the sheath edge toward the wall. This field repels negatively charged dust particles, increasing the dust density near the sheath boundary. The higher dust density may also contribute to the observed rise in ion concentration at the sheath edge. Figures 6 and 7 show the corresponding normalized velocities of He^+ ion (figure 3) and Ar^+ ions (figure 4) as a function of normalized distance. The velocity profiles exhibit an inverse relationship to the density profiles, ensuring flux conservation.

4.2. *Ion–neutral collisional effect with ionization*

This section discusses the effects of ion–neutral collisions with ionization on the He^+ and Ar^+ ion densities. Figures 8 and 9 show the normalized density profile as a function of normalized distance for He^+ and Ar^+ ions, respectively. From both figures, it is evident that, as the ion–neutral collision frequency increases, ion density tends to accumulate near the sheath edge, and the density peaks become narrower with higher collisional force. This is because the decelerating effect of collision forces on ions outweighs the accelerating effect of the electric force. As a result, the positive ions slow down, leading to their accumulation. The narrowing is

https://doi.org/10.1017/S0022377825100755 Published online by Cambridge University Press

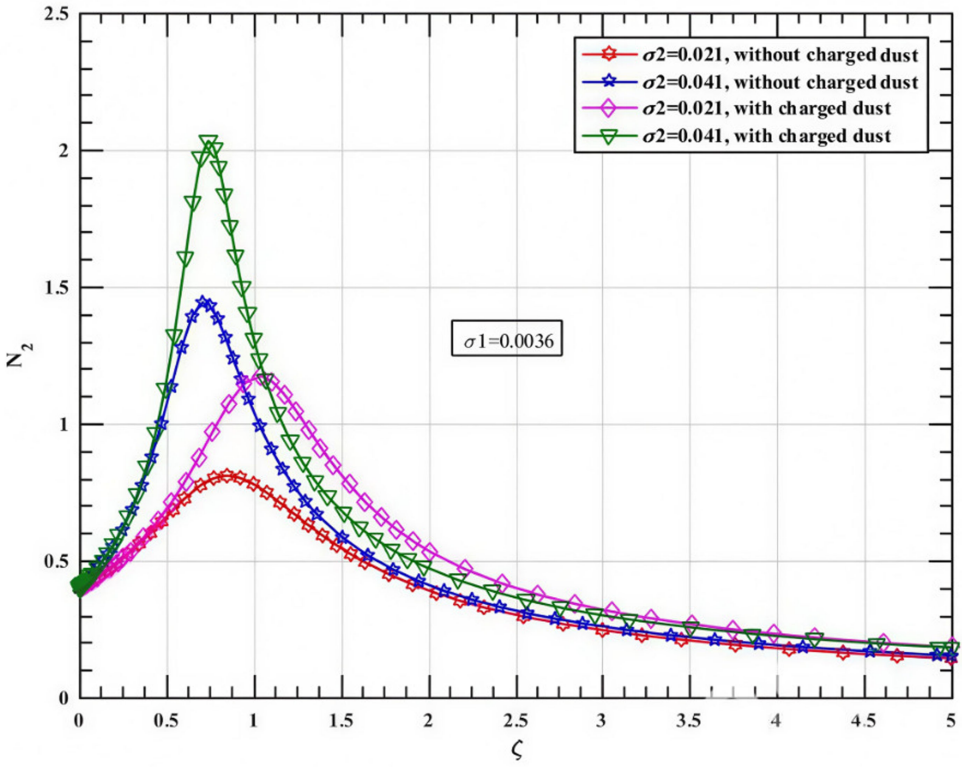

FIGURE 4. Variation of normalized Ar^+ ion density with normalized distance for different values of σ, and the other physical variables are the same as figure 3.

more pronounced for Ar^+ ions than for He^+ ions because argon has a larger collision cross-section leading to more frequent collisions and increased ion bunching. Furthermore, He^+ ions possess a higher diffusion coefficient ($\sim\propto 1/m$) compared with Ar^+ ions. Additionally, in the presence of a magnetic field (with $\beta = 1.5$ and $\theta = 10^0$), He^+ ions, both in the presence and absence of dust particles, begin to gyrate with a gyro-radius of 0.236 mm. Concurrently, they exhibit a drift in the direction of the wall, driven by the $E \cdot B$ drift velocity, given approximately by $v_d^{E\cdot B} \approx (E \cdot B)/B^2$. As a result, these combined effects contribute to a broader He^+ ion density profile that extends further toward the wall.

4.3. *Impact of non-thermal electrons on ion densities and potential*

Figure 10 illustrates the influence of non-thermal electrons (b) on the sheath potential as a function of normalized distance. Non-thermal electrons, which exhibit a non-Maxwellian energy distribution, possess higher energies compared with thermal electrons, enabling them to overcome the sheath potential barrier more effectively. As their population increases, the electron flux toward the boundary (wall) rises significantly, leading to an enhanced electron current. To maintain charge balance, where the ion and electron currents to the surface must be equal, the sheath potential increases to counteract the additional electron flux. This results in a more negative sheath potential, which intensifies the electric field within the sheath region. The

https://doi.org/10.1017/S0022377825100755 Published online by Cambridge University Press

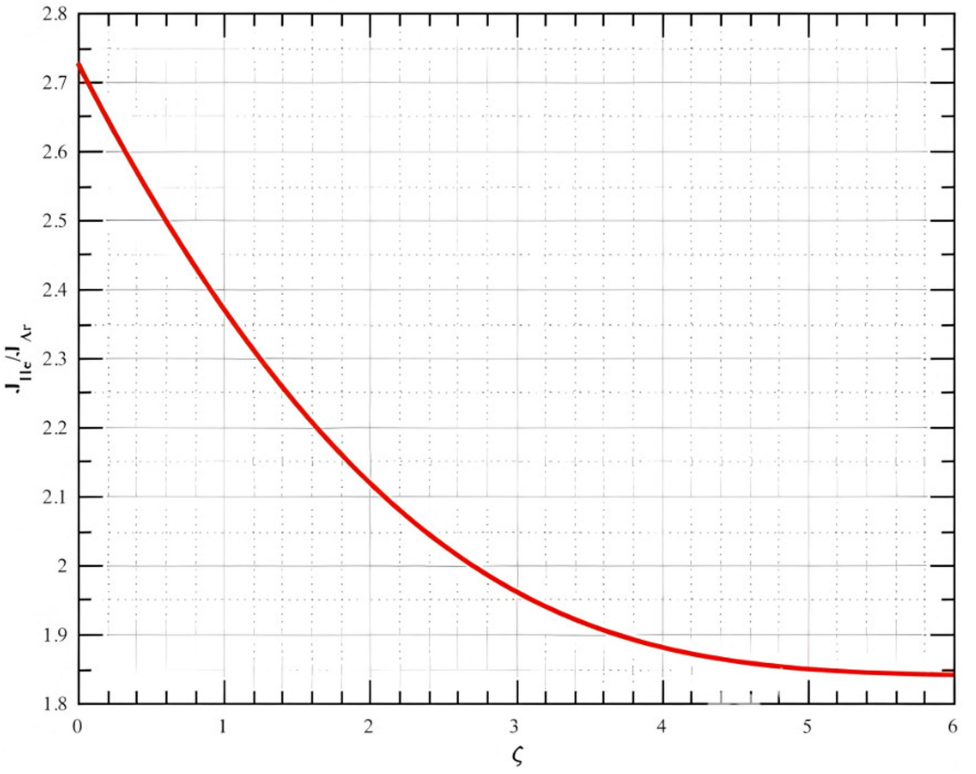

FIGURE 5. Normalized current profile function of normalized distance.

increased sheath potential ensures that sufficient ions are attracted to the boundary to balance the higher electron flux, thereby preserving plasma–wall equilibrium.

The normalized ion density profiles of He^+ and Ar^+ ions as a function of normalized distance are shown in figures 11 and 12, respectively. It is evident from the figures that, as the non-thermal electron population increases, the ion densities initially rise near the sheath edge and then decline for both ion types. This behaviour occurs because the rise in the non-thermal electron population enhances electron–neutral ionization processes, leading to greater ion production near the sheath edge. Non-thermal electrons, with their higher energies, significantly increase ionization rates. However, as ions are accelerated toward the wall by the sheath electric field and undergo ion–neutral collisions, their density declines further into the sheath. Additionally, the ion density also decreases in the presence of negatively charged dust for a specific population of non-thermal electrons, as shown in figure 13. This balance between ionization (source) and ion loss (sink) results in the observed initial rise and subsequent decline in ion density.

4.4. *Ionization effect on electron density, sheath potential and space charge*

The effect of normalized ionization frequency (σ) on the electron density distribution is analysed while keeping other parameters constant, as shown in figure 14. The profile suggests that more electrons are consumed as ionization increases, leading to a sharp decrease in electron density within the sheath. Figure 15 illustrates the dynamic of normalized sheath potential as a function of normalized distance for

https://doi.org/10.1017/S0022377825100755 Published online by Cambridge University Press

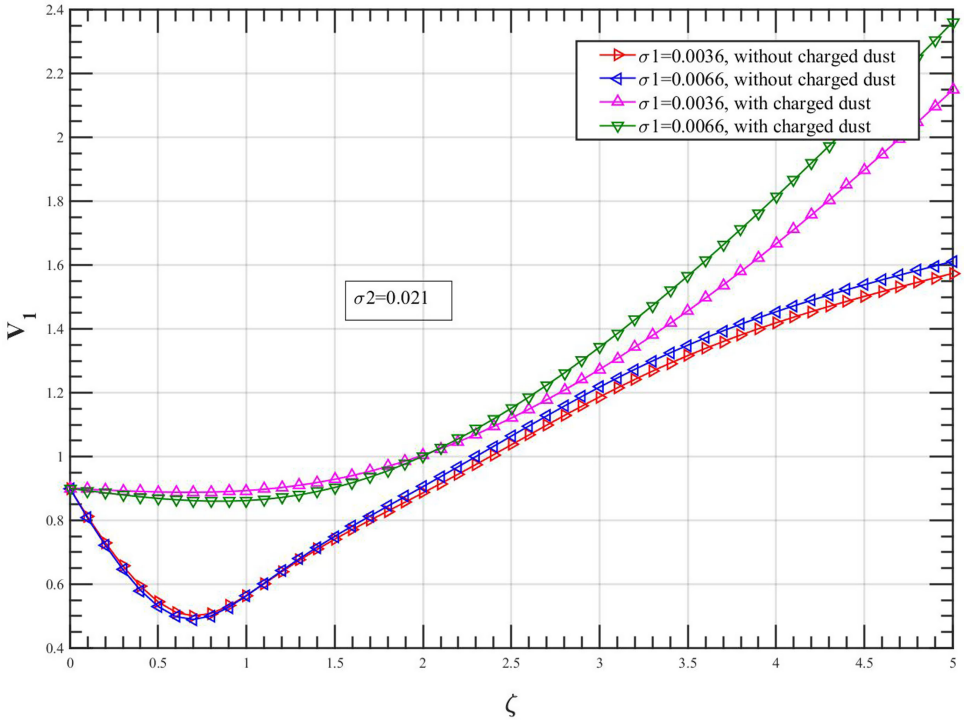

FIGURE 6. Variation of normalized He^+ ion velocity with normalized distance for different values of σ, and the other physical variables are the same as figure 3.

different values of σ. Figure 16 shows that, as the value of σ increases (indicating a larger ionization source), the sheath thickness becomes significantly narrower. This can be explained by the fact that increased ionization leads to a higher production of positive ions, which move toward the negatively charged wall. Consequently, the electric potential profile steepens more quickly, causing ions to accumulate within a more confined region.

Figure 16 demonstrates the normalized space charge in relation to normalized distance. It reveals that the space charge migrates toward the sheath edge with increasing ionization frequency. This phenomenon arises because the density of electrons decreases more rapidly while the density of positive ions initially declines at a slower space. As a result, the space charge attains a peak value, indicating a build-up of positive particles that effectively neutralizes the negative potential created by the charged dust and the wall.

4.5. *Magnetic field and orientation impact on ion density*

Figures 17 and 18 illustrate the normalized ion density variations of He^+ and Ar^+ ions as a function of normalized distance for constant magnetic field angle, respectively. Both figures show that, with an increase in the magnetic field, the ion densities for both species exhibit pronounced peaks and narrow distributions. With the increase in magnetic field strength, the gyro-radius of the ions decreases, as the gyro-radius is inversely proportional to the magnetic field strength ($\rho_i \propto \beta^{-1}$),

https://doi.org/10.1017/S0022377825100755 Published online by Cambridge University Press

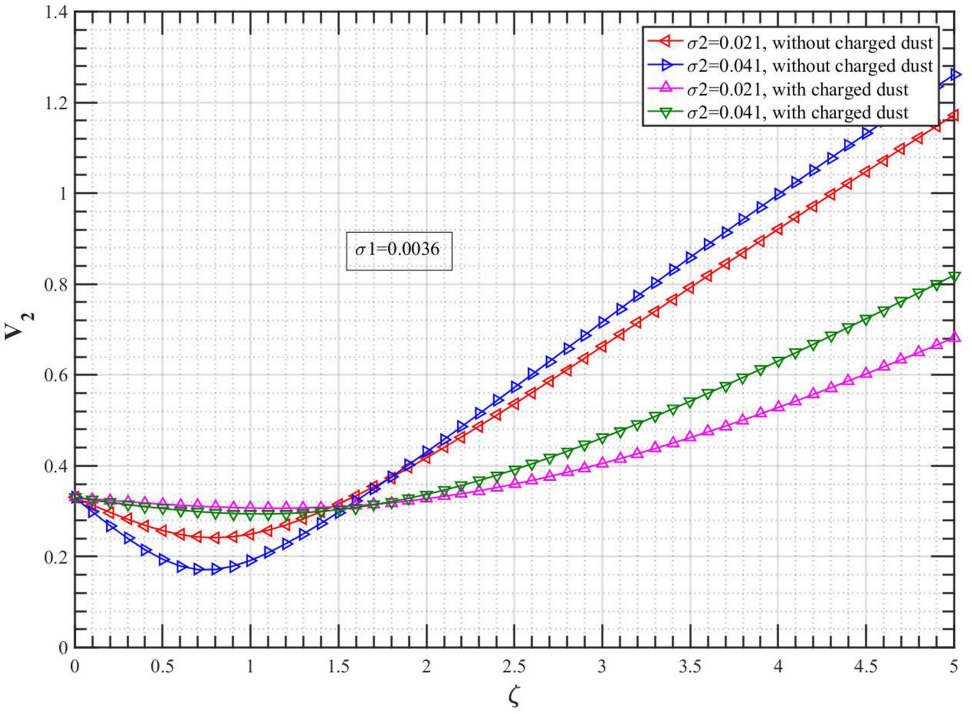

FIGURE 7. Variation of normalized Ar^+ ion velocity with normalized distance for different values of σ, and the other physical variables are the same as figure 3.

hence the sharpness of the density peak is observed towards the sheath edge. For the magnetic fields of 0.5 and 1.5, the gyro-radii of He^+ and Ar^+ ions are calculated. For the magnetic field strength (β) of 0.5, the gyro-radii of He^+ and Ar^+ ions are 0.120 and 0.235 mm, respectively. When β increases to 1.5 the gyro-radii of He^+ and Ar^+ ions decrease to 0.0401 and 0.0786 mm, respectively. This reduction indicates that, as the *B*-field strength increases, the gyro-radius becomes smaller, implying that the space-averaged ion density tends to be enhanced. Consequently, ions are confined to tighter circular orbits around the *B*-field lines, resulting in more constrained gyro-motion. The shifting of peaks towards the sheath edge can be explained by figure 19.

Figure 19 presents the net ion density variation inside the sheath as a function of normalized distance for the constant magnetic field. We vary the magnetic field incidence angle is in the range $\theta = 5^\circ - 55^\circ$ keeping the magnetic field strength the same ($\beta = 1$). It is observed that the density peak shifts towards the sheath edge with the increase of the angle of incidence. The magnetic field is allowed to intercept the wall at an angle θ heaving horizontal components ($B_z = B_0 \cos\theta\hat{z}$) and vertical components ($B_x = B_0 \sin\theta\hat{x}$) . At $\theta = 0^\circ$, the loss of ions towards the wall is maximum. The vertical component of the magnetic field increases, followed by the decrease in the horizontal component with the increase in θ. Thus, the ion loss decreases along the horizontal direction, therefore, the ion density begins to peak in the vertical direction, and its amplitude tends to increase proportionally to the magnetic field strength.

https://doi.org/10.1017/S0022377825100755 Published online by Cambridge University Press

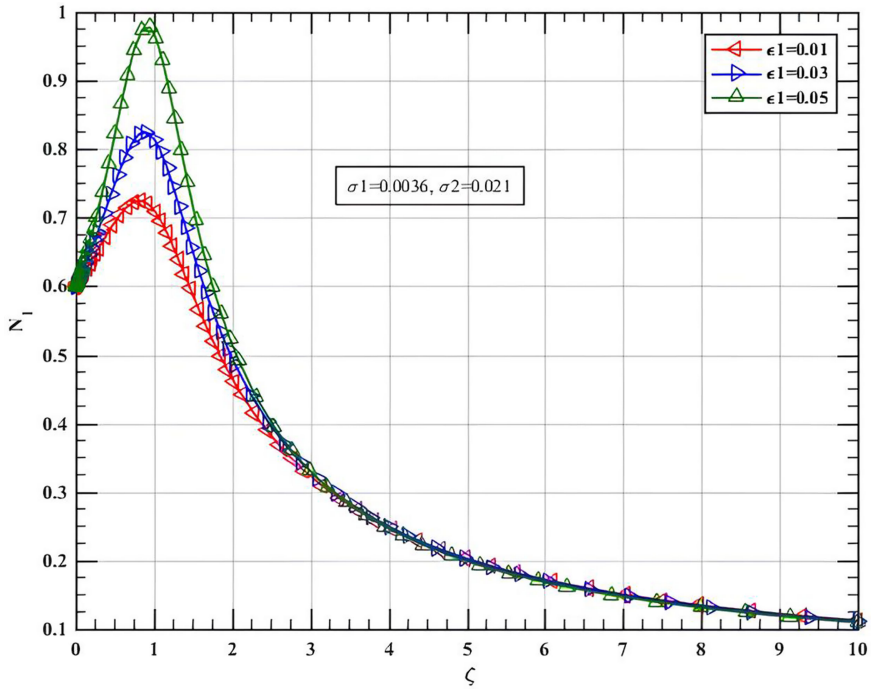

FIGURE 8. Variation of normalized He^+ ion density with normalized distance for different values of ϵ, and the other physical variables are the same as figure 3.

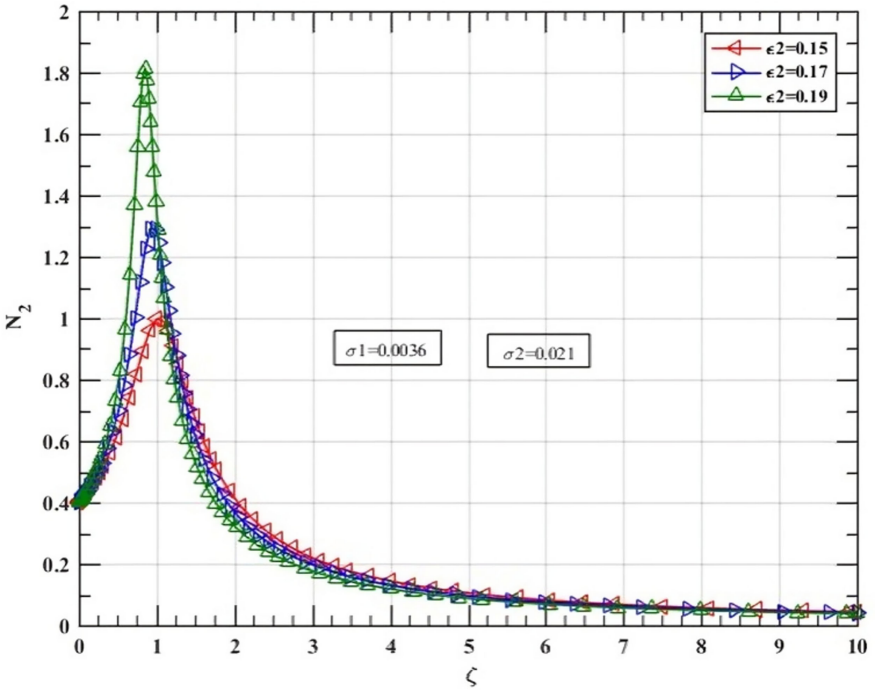

FIGURE 9. Variation of normalized Ar^+ ion density with normalized distance for different values of ϵ, and the other physical variables are the same as figure 3.

https://doi.org/10.1017/S0022377825100755 Published online by Cambridge University Press

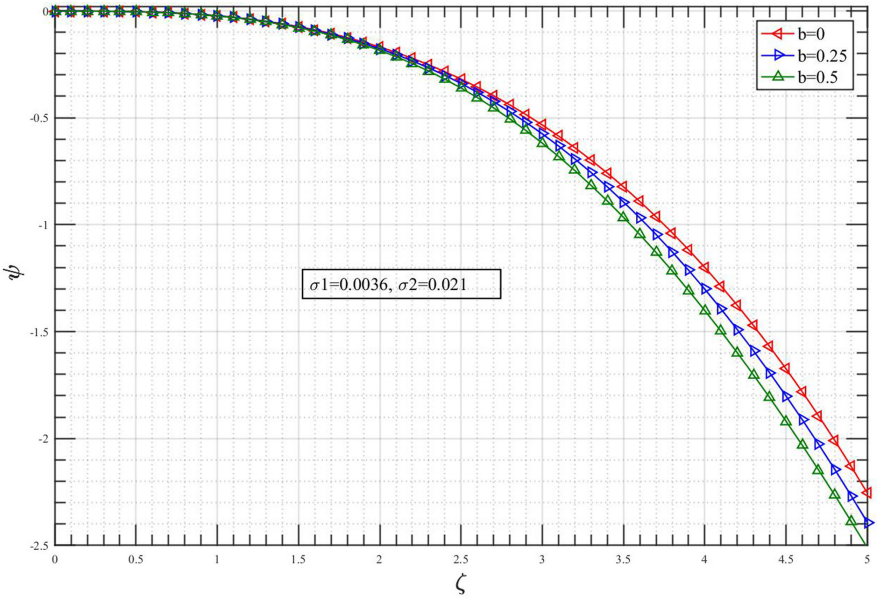

FIGURE 10. Variation of normalized sheath potential with normalized distance for different values of b, and the other physical variables are the same as figure 3.

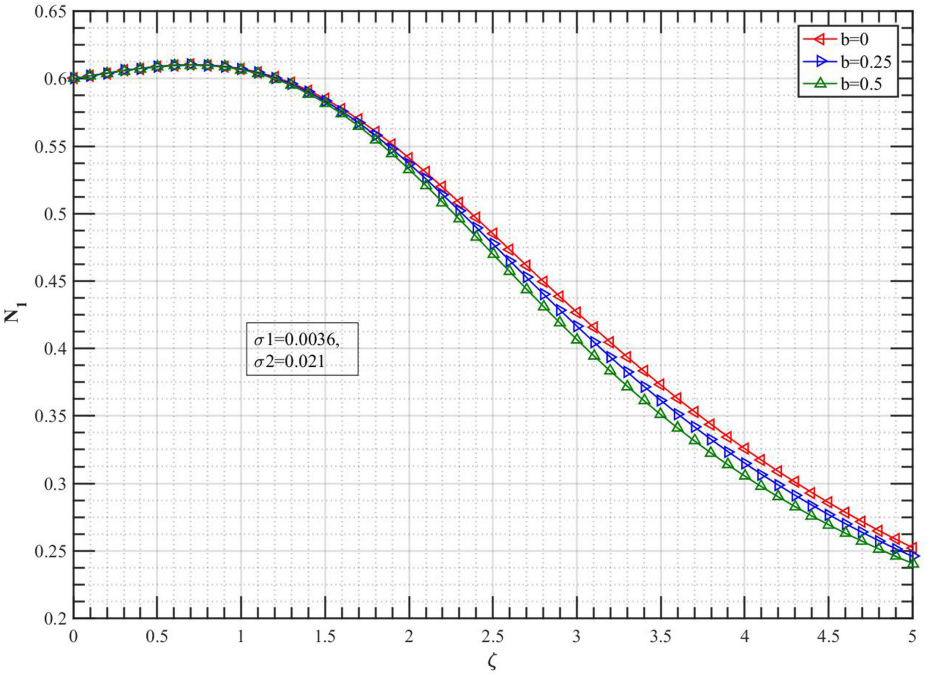

FIGURE 11. Variation of normalized He^{+} ion density with normalized distance for different values of b, and the other physical variables are the same as figure 3.

https://doi.org/10.1017/S0022377825100755 Published online by Cambridge University Press

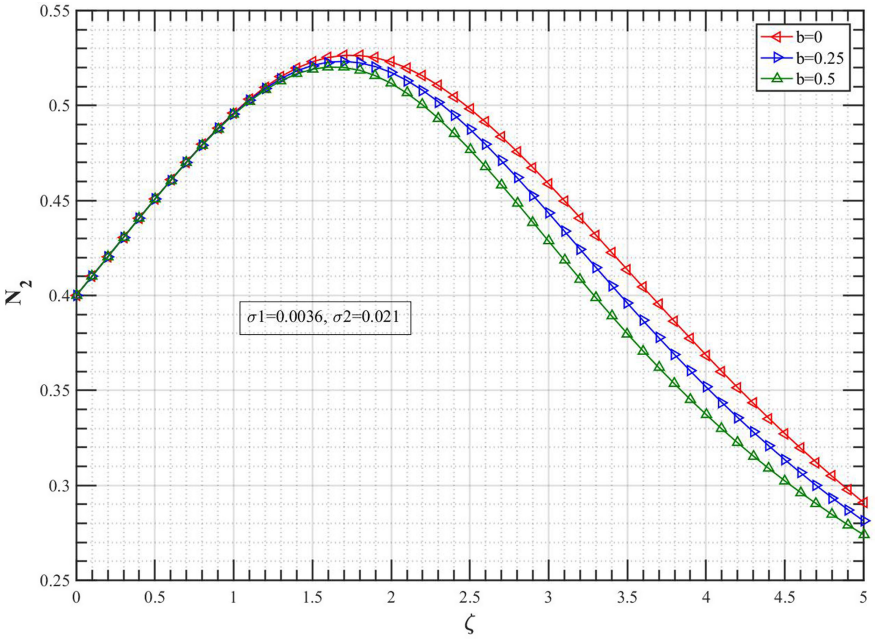

FIGURE 12. Variation of normalized Ar^+ ion density with normalized distance for different values of b, and the other physical variables are the same as figure 3.

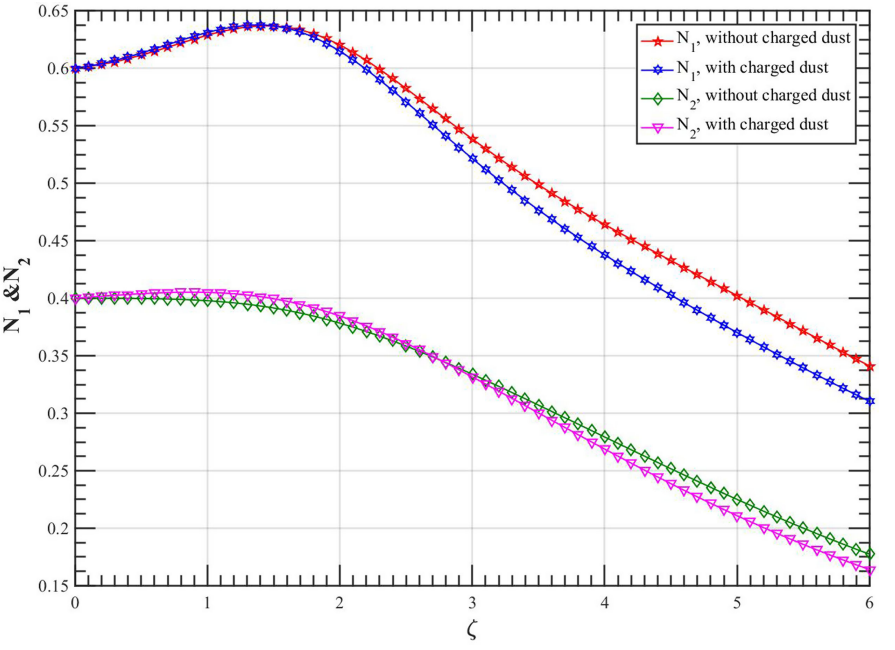

FIGURE 13. Variation of normalized He^+ and Ar^+ ion density with normalized distance in presence and absence of charged dust for a constant values of b, and the other physical variables are the same as figure 3.

https://doi.org/10.1017/S0022377825100755 Published online by Cambridge University Press

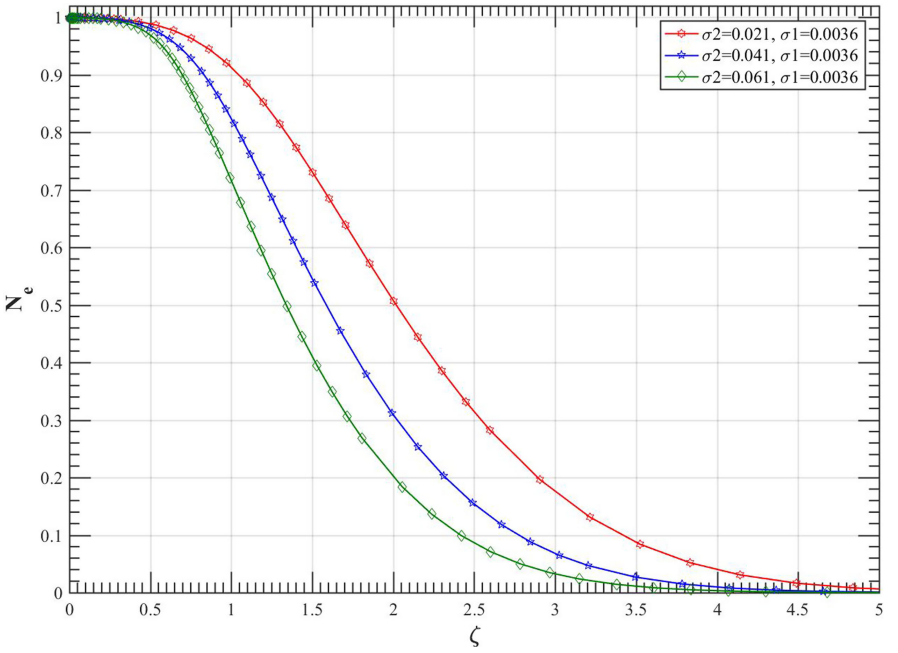

FIGURE 14. Normalized electron density as a function of normalized distance with varying σ, and the other physical variables are the same as figure 3.

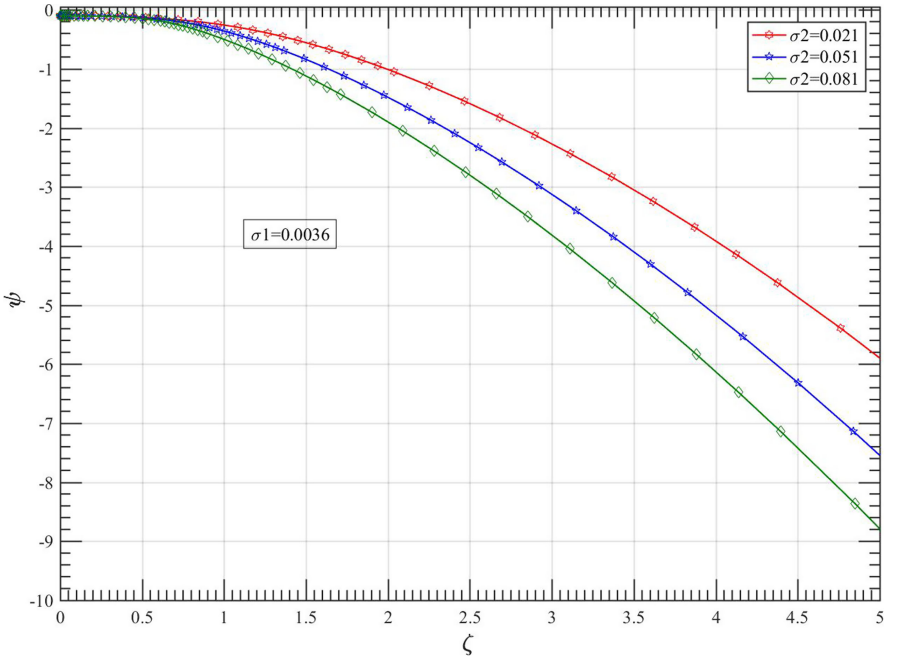

FIGURE 15. Variation of normalized sheath potential with normalized distance for different values of σ, and the other physical variables are the same as figure 3.

https://doi.org/10.1017/S0022377825100755 Published online by Cambridge University Press

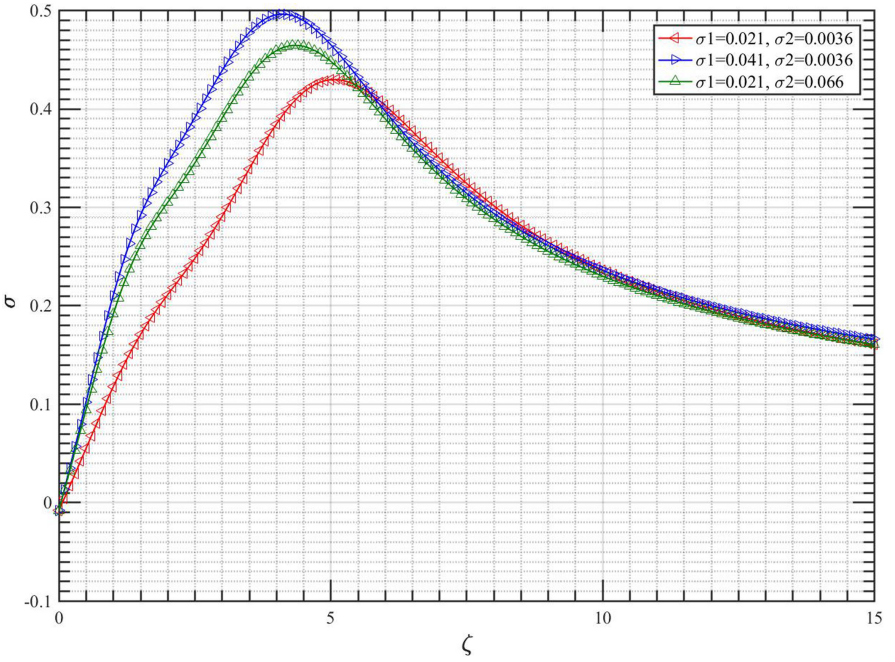

FIGURE 16. Variation of space charge with normalized distance for different values of σ, and the other physical variables are the same as figure 3.

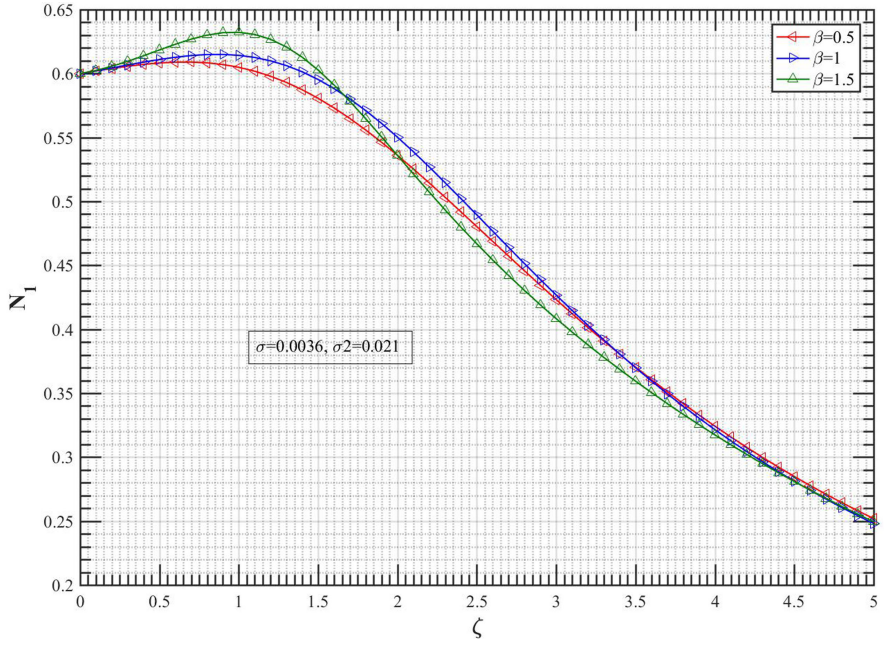

FIGURE 17. Variation of normalized He^+ ion density with normalized distance for different values of β, and the other physical variables are the same as figure 3.

https://doi.org/10.1017/S0022377825100755 Published online by Cambridge University Press

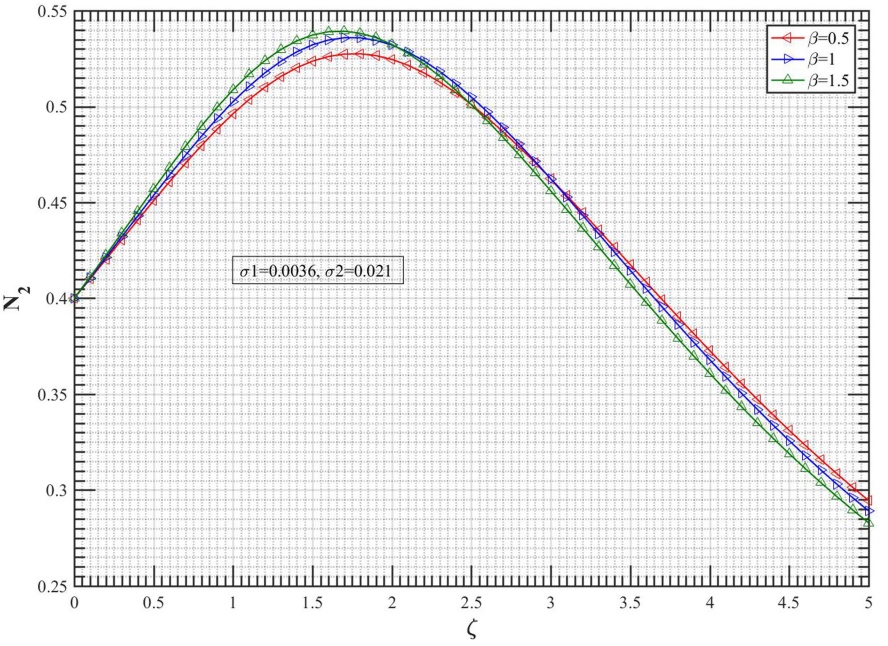

FIGURE 18. Variation of normalized Ar^+ ion density with normalized distance for different values of β, and the other physical variables are the same as figure 3.

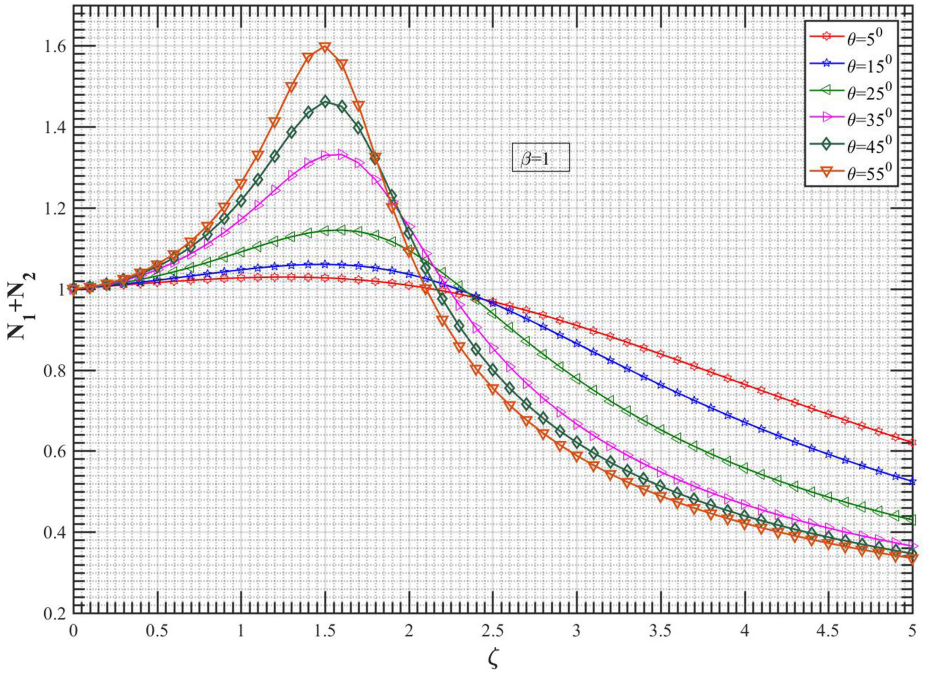

FIGURE 19. Net ion ($He^+ + Ar^+$) density profile as function of normalized sheath thickness with varying θ and the other parameters are same with figure 3.

https://doi.org/10.1017/S0022377825100755 Published online by Cambridge University Press

5. Summary

The behaviour of a collisional magnetized plasma sheath with two positive ion species, non-thermal electrons and negatively charged dust is studied under electron impact ionization, ion–neutral collisions and an external magnetic field. The dynamics of helium and argon ion densities, with and without charged dust, is analysed for varying ionization frequencies. Sheath potential, electron density, ion flux and space charge are evaluated, along with the effects of non-thermal electrons and the *B*-field on electron and ion densities.

i. With increased electron impact ionization, He^+ and Ar^+ ion densities rise due to enhanced ion production, increasing the sheath ion density. Charged dust in the sheath reduces the He^+ ion density but increases the Ar^+ ion density. The He^+ ion decline is due to a stronger dust charge near the sheath edge, as lighter He^+ ions generate higher dust charging currents, consuming more ions. Increased ion loss frequency further decreases helium ions.

ii. As σ increases, sheath potential decreases, indicating stronger ionization and narrowing of the sheath. Higher ionization produces more positive ions moving toward the negatively charged wall, steepening the electric potential and confining ions to a smaller region.

iii. Density peaks appear with increasing ion–neutral collision frequency and narrow with stronger collisional forces. Ion–neutral collisions restrict ion motion toward the wall and hinder acceleration by the electric field. This effect is more pronounced for Ar^+ ions, which have a larger collision cross-section than He^+ ions, causing more collisions and greater ion bunching.

iv. Higher non-thermal electrons (b) leads to more energetic electrons reaching the wall, making it more negative and increasing the sheath potential. This also extends the sheath region, as sheath thickness depends on electrostatic potential, plasma density, and ion-entering velocity.

v. Ion density peaks with an increase in *B*-field due to a smaller ion gyro-radius, confining ions to tighter orbits around the *B*-field lines. The shift in ion peaks is due to the magnetic field's inclination.

vi. In this study, we adopted a 1-D simplified sheath model, assuming an arbitrary electric field at the sheath edge and neglecting transverse ion velocities (u_x and u_y). However, as noted by Valentin (2000), the electric field at the sheath edge should have a well-defined value rather than an arbitrary one. In our future work, we plan to extend the study to a 3-D model by considering non-zero transverse ion velocities and a definite value of the electric field.

The results of our research hold significant technological value for numerous applications involving low-temperature plasmas where dust particles are commonly found.

Acknowledgements

Authors express their special thanks of gratitude to Dr A.K. Sanyasi, Institute for Plasma Research, Gujarat, India for his valuable suggestions and discussion.

Editor Edward Thomas, Jr. thanks the referees for their advice in evaluating this article.

Declaration of interests

The authors report no conflict of interest.

REFERENCES

BASNET, S., SARMA, A. & KHANAL, R. 2020 Effect of presheath electron temperature on magnetized plasma-wall transition and wall sputtering by plasma having two species of positive ions. *Phys. Scr.* **95**, 065601.

BOSTROM, R. 1992 Observations of weak double layers on auroral field lines. *IEEE Trans. Plasma Sci.* **20**, 756.

CAIRNS, R.A., MAMUM, A.A., BINGHAM, R., BINGHAM, R., R.O.DENDY, O., NAIRN C.M., C. & SHUKLA, P.K. 1995 Electrostatic solitary structures in non-thermal plasmas. *Geophys. Res. Lett.* **22**, 2709.

CHEKOUR, S., TAHRAOUI, A. & ZAHAM, B. 2012 Effects of fast monoenergetic electrons on the generalized Bohm criterion for electronegative dusty plasma. *Phys. Plasmas* **19**, 053502.

CHEN, L., YANG, YH., AN, Y.H., DUAN, P., SUN, S.J., CUI, Z.J., KAN, Z.C. & GAO, W.F. 2023 Multi-ion magnetized sheath properties with non-extensive electron distribution. *Plasma Sci. Technol.* **25**, 035003.

DHAWAN, R. & MALIK, H.K. 2023 Sheath formation mechanism in collisional electronegative warm plasma with two-temperature non-extensive distributed electrons and ionization. *J. Appl. Phys.* **133**, 043303.

DUBINOV, A.E. 2009 On a widespread inaccuracy in defining the mach number of solitons in a plasma. *Plasma Phys. Rep.* **35**, 991.

EL BOJADDAINI, M. & CHATEI, H. 2020 Investigation of magnetized plasma Sheath in the presence of non-extensive electrons and ionization source. *Eur. Phys. J. Plus* **135**, 680.

FOROUTAN, G. 2010 Fluid simulation of an electrostatic plasma sheath with two species of positive ions and charged nanoparticles. *Phys. Plasmas* **17**, 123711.

FOROUTAN, G. & AKHOUNDI, A. 2012 Investigation of the sheath formation in a dusty plasma containing energetic electrons and nano-size dust grains. *Phys. Plasmas* **19**, 103505.

FOUIAL, N., TAHRAOUI, A. & ANNOU, R. 2016 Bohm criterion in dusty plasmas with two species of positive ions and non-thermal electrons. *Phys. Plasmas* **23**, 113702.

FRANKLIN, R.N. 2003 The plasma–sheath boundary region. *J. Phys. D: Appl. Phys.* **36**, R309.

FRANKLIN, N. 2003 The plasma-sheath and its stability in a quiescent plasma containing two species of positive ion. *J. Phys. D: Appl. Phys.* **36**, 1806.

FRANKLIN, R.N. 2005 The active magnetized plasma-sheath over a wide range of collisionality. *J. Phys. D: Appl. Phys.* **38**, 3412.

FRANKLIN, R.N. & OCKENDON, J.R. 1970 Asymptotic matching of plasma and sheath in an active low pressure discharge. *J. Plasma Phys.* **4**, 371.

HATAMI, M.M. 2015 An analytic expression for the sheath criterion in magnetized plasmas with multi-charged ion species. *Phys. Plasmas* **22**, 043510.

HATAMI, M.M., NIKNAM, A.R., SHOKRI, B. & GHOMI, H. 2008 Magnetized plasma sheath with two species of positive ions. *Phys. Plasmas* **15**, 053508.

HATAMI, M.M., SHOKRI, B. & NIKNAM, A.R. 2009 Collisional effects in magnetized plasma sheath with two species of positive ions. *J. Phys. D: Appl. Phys.* **42**, 025204.

IVLEV, A.V. & MORFILL, G. 2000 Acoustic modes in a collisional dusty plasma: Effect of the charge variation. *Phys. Plasmas* **7**, 1094.

KHALILPOUR, H. & FOROUTAN, V. 2020 Numerical study of an electrostatic plasma sheath with non-thermal electrons and charged nanoparticles. *Contrib. Plasma Phys.* **60**, e201900060.

KONG, J., *et al.* 2016 Temperature measurement of a dust particle in a RF plasma GEC reference cell. *J. Plasma Phys.* **82**, 905820505.

LIEBERMAN, M.A. & LICHTENBERG, A.J. 2005 *Principles of Plasma Discharges and Materials Processing*. Wiley.

LIU, J.Y., WANG, D. & MA, T.C. 2000 The charged dust in processing plasma sheath. *Vacuum* **59**, 126.

MAIOROV, S.A., KODANOVA, S.K., DOSBOLAYEV, M.K., RAMAZANOV, T.S., GOLYATINA, R.I., BASTYKOVA, N.K. & UTEGENOV, A.U. 2015 The role of gas composition in plasma-dust structures in RF discharge. *Phys. Plasmas* **22**, 033705.

MISRA, A.P. & CHOWDHURY, A.R. 2004 Acoustic surface waves in a collisional dusty plasma. *Physica Scr.* **69**, 44.

MAND, D. & MASHAYEK, F. 2005 Dust particle dynamics in magnetized plasma sheath. *Phys. Plasmas* **12**, 073505.

MEHDIPOUR, H., DENYSENKO, I. & OSTRIKOV, K. 2010 Magnetized collisional sheath. *Phys. Plasmas* **17**, 12370.

MERLINO, R.L. 2006 Effect of electron and/or ion nonthermality on dust acoustic wave propagation in a complex plasma in presence of positively charged dust grains generated by secondary electron emission process. *Plasma Phys. Appl.* 73–110.

MERLINO, R. 2021 Dusty plasmas: from Saturns rings to semiconductor processing devices. *Adv. Phys.: X* **6**, 1873859.

OU, J., GAN, C., LIN, B. & YANG, J. 2015 The magnetized sheath of a dusty plasma with grains size distribution. *Phys. Plasmas* **22**, 053705.

OU, J. & MEN, Z.Z. 2020 Formation of the radio frequency sheath of plasma with Cairns-Tsallis electron velocity distribution. *Phys. Plasmas* **27**, 083517.

RAFFAH, B.M., ABID, A.A., KHAN, A., AL-HADEETHI, Y. & QURESHI, M.N.S. 2024 Dust particle surface potential in an argon-helium plasma using the (r,*q*)-distribution function. *Commun. Theor. Phys.* **76**, 095501.

RESENDES, D.P., SORASIO, G. & SHUKLA, P.K. 2002 Dynamics of dust particles in plasma sheaths. *Phys. Plasmas* **9**, 2988.

RIEMANN, K.U. 1991 The Bohm criterion and Sheath formation. *J. Phys. D: Appl. Phys.* **24**, 493.

RIEMANN, K.U. 1992 Kinetic theory of plasma sheaths. *J. Phys. D: Appl. Phys.* **25**, 1432.

RIEMANN, K.U. 1997 The influence of collisions on the plasma sheath transition. *Phys. Plasmas* **4**, 4158–4166.

RIEMANN, K.-U. 2003 Kinetic analysis of the collisional plasma–sheath transition. *J. Phys. D: Appl. Phys.* **36**, 2811.

RIEMANN, K.U., SEEBACHER, J., TSKHAKAYA, D.D. & KUHN, S. 2005 The plasma–sheath matching problem. *Plasma Phys. Control Fusion* **47**, 1949.

SADATIAN, S.D. & GHIYAEI, M.G. 2021 Generalized Bohm sheath criterion in dusty plasma of space environment, Adv. *Space Res.* **68**, 3455.

SHAW, A.K., KAR, S. & GOSWAMI, K.S. 2012 The positive ion temperature effect in magnetized electronegative plasma sheath with two species of positive ions. *Phys. Plasmas* **19**, 102108.

SHAW, A.K., KAR, S., GOSWAMI, K.S. & SAIKIA, B.J. 2012 Numerical investigation of the ion temperature effect in magnetized plasma sheath with two species of positive ions. *Phys. Plasmas* **19**, 012120.

SHAW, A.K., SANYASI, A.K. & KAR, S. 2023 Study of magnetized multi-component plasma sheath containing charged dust particles in presence of oblique magnetic field: a fluid approach. *Phys. Scr.* **98**, 015606.

SHAW, A.K., SANYASI, A.K. & SHARMA, D. 2024 Magnetized multi-component plasmas sheath characteristics with three isothermal ion species. *Phys. Scr.* **99**, 085610.

SHERIDAN, T.E. & GOREE, J. 1991 Collisional plasma sheath model. *J. Phys. Fluids B* **3**, 2796.

SINGHA, B., SARMA, A. & CHUTIA, J. 2001 Influence of magnetic field on plasma sheath and electron temperature. *Rev. Sci. Instrum.* **72**, 2282–2287.

TAMANG, J., SARKAR, K. & SAHA, A. 2018 Solitary wave solution and dynamic transition of dust ion acoustic waves in a collisional nonextensive dusty plasma with ionization effect. *Phys. Scr. A* **505**, 18.

TANG, X.Z. & DELZANNO, G.L. 2014 Orbital-motion-limited theory of dust charging and plasma response. *Phys. Plasmas* **21**, 123708.

VALENTIN, H.B. 2000 Sheath formation in low-pressure discharges. *Plasma Sources Sci. Technol.* **9**, 574–582.

ZHAO, X., ZHANG, B. & WANG, C. 2020 Dust charging and levitating in a magnetized plasma sheath containing superextensive electrons. *Phys. Plasmas* **27**, 113705.

ZOU, X., LIU, J.-Y., GONG, Y., WANG, Z.-X., LIU, Y., WANG, X.-G. 2004 Plasma sheath in a magnetic field. *Vacuum* **73**, 681–685.

https://doi.org/10.1017/S0022377825100755 Published online by Cambridge University Press